



Construction of homojunction-adsorption layer on anatase TiO₂ to improve photocatalytic mineralization of volatile organic compounds



Jinze Lyu ^{a,b,c,*}, Junxian Gao ^a, Min Zhang ^a, Qiang Fu ^a, Luna Sun ^a, Shuang Hu ^a, Junbo Zhong ^d, Shuo Wang ^{a,b,c}, Ji Li ^{a,b,c}

^a School of Environment and Civil Engineering, Jiangnan University, Wuxi, Jiangsu, 214122, China

^b Jiangsu Key Laboratory of Anaerobic Biotechnology, Jiangnan University, Wuxi, Jiangsu, 214122, China

^c Jiangsu College of Water Treatment Technology and Material Collaborative Innovation Center, Suzhou, Jiangsu, 215009, China

^d Key Laboratory of Green Catalysis of Higher Education Institutes of Sichuan, College of Chemistry and Pharmaceutical Engineering, Sichuan University of Science and Engineering, Zigong, Sichuan, 643000, China

ARTICLE INFO

Article history:

Received 21 June 2016

Received in revised form 27 August 2016

Accepted 21 September 2016

Available online 22 September 2016

Keywords:

Homojunction

Micropore

Charge carriers

VOCs

Mineralization

ABSTRACT

The separation and injection of photogenerated charge carriers significantly affect the mineralization efficiency of volatile organic compounds (VOCs). These two processes can be optimized by enhancing the separation of charge carriers and the adsorption of VOCs via material engineering. However, obtaining both high adsorption ability and photoactivity of VOCs simultaneously at the ppm level is difficult. In this work, we grew microporous TiO₂ onto the surface of anatase TiO₂ to construct a homojunction-adsorption layer, enhancing both the adsorption and photodegradation of low concentration of toluene, which was chosen as model VOC. N₂ adsorption/desorption, transmission electron microscopy, X-ray diffraction, X-ray photoelectron spectroscopy (XPS), GC-flame ionization detection, and surface photovoltage spectroscopy (SPS) were employed to analyze the physical properties and mineralization of toluene. Results showed that growth of microporous TiO₂ increased the surface area of the catalyst by 160% compared with anatase TiO₂, as well as induced microporous structure. This phenomenon significantly enhanced the adsorption of toluene at a low concentration of 5.5 mg/m³ and limited the release of the adsorbed organic compounds. Moreover, SPS and XPS results proved that a homojunction was constructed at the interface of microporous TiO₂ and anatase TiO₂, greatly improving the separation of photogenerated charge carriers. Owing to the enhanced adsorption ability and photoactivity, the mineralization efficiency of toluene over micropore-anatase TiO₂ composite was 1.78 and 2.12 times higher than that over M-TiO₂ and anatase TiO₂, respectively.

© 2016 Elsevier B.V. All rights reserved.

1. Introduction

Volatile organic compounds (VOCs) are a group of ubiquitous air pollutants. They can cause acute and chronic respiratory disease, heart disease, and even cancer [1]. VOCs are a crucial precursor of tropospheric PM2.5, which poses major environmental challenges that are currently faced by developing countries, such as China and India [2–4]. Photocatalysis using TiO₂ is one of the most promising technologies employed to control both indoor and industrial VOCs. However, this technology can only be promoted once its mineralization efficiency is improved and its release of toxic byproducts is diminished.

Photocatalytic mineralization of VOCs is mainly controlled by three processes, namely, light harvesting, photogenerated charge carrier (electrons and holes) separation, and charge injection from catalyst surface into VOCs and its intermediates. Light harvesting is not a major problem given that high-energy and high-intensity UV light is easily used in photocatalytic equipment. Techniques such as metal doping, nonmetallic element doping, and formation of heterojunction from different substances with matched energy bands to enhance the separation efficiency of charge carriers have been used [5–9]. However, in practical application, the use of photocatalysts that demonstrate high separation efficiency of charge carriers is insufficient to achieve high mineralization efficiency. This phenomenon is largely caused by low VOC concentrations (ppb–ppm) in most environmental cases [10–12]. VOCs at such low level cannot be efficiently absorbed by conventional catalysts, and the formed intermediates are easily desorbed from the surface of catalysts to become byproducts [13]. With a relatively low VOC

* Corresponding author at: School of Environment and Civil Engineering, Jiangnan University, Wuxi, Jiangsu, 214122, China.

E-mail address: ljz@jiangnan.edu.cn (J. Lyu).

concentration on catalyst surface, a large proportion of photogenerated charge carriers will recombine rather than become injected into VOCs to induce redox reaction, resulting in low mineralization efficiency. Coating catalysts on adsorbents containing micropores, such as active carbon and zeolite, can enhance the removal of some kinds of VOCs [14–16]. After separation of the adsorption sites and photocatalytic sites of the adsorbent-supported catalysts, removal efficiency becomes dependent on the selectivity of the adsorbent to VOCs and on the transfer rate of VOCs from adsorption sites to photocatalytic sites [17]. Another means to enhance VOC adsorption is to prepare porous catalysts with large surface area. Increased surface area would induce more adsorption sites and thus enhances VOC adsorption. Researchers currently focus mainly on mesoporous catalysts that exhibit both large surface area and high crystallinity. Lee and his coworkers synthesized ordered mesoporous TiO₂ with high crystallinity via CASH method [18]. Zhao constructed SiO₂ and TiO₂ to form highly ordered hexagonal mesoporous crystalline TiO₂-SiO₂ nanocomposites [19]. However, in most cases of VOC pollution (at the ppb and ppm levels), the physical adsorption ability of mesopores is much weaker than that of micropores. This phenomenon is observed because the adsorption potentials of adjacent pore walls overlap to form a new stronger one with a pore size of <2 nm (micropore) [20,21]. Microporous materials, such as active carbon, are widely used to purify either indoor air or industrial air because of their outstanding adsorption ability for low VOC concentration. In our previous work [22,23], we synthesized microporous TiO₂ with an average pore size of approximately 1.2 nm. The micropores greatly enhanced the adsorption of toluene and cyclohexanone at 1 mg/m³ concentration, improving the photocatalytic degradation efficiency. However, the low crystallinity of microporous TiO₂ significantly limits the photoactivity of the catalyst. In addition, formation of microporous TiO₂ with high crystallinity is very difficult to achieve because the crystallization is accompanied by the collapse of micropores. Our previous result suggested that obtaining both high adsorption ability for low VOC concentration and high separation efficiency of charge carriers are feasible by forming a complex using crystal TiO₂ and microporous TiO₂. Moreover, because of the different arrangements of Ti and O atoms in crystal TiO₂ and microporous TiO₂ (amorphous pattern), the crystal-micropore TiO₂ composite may exhibit some special optical characteristics. To our knowledge, few studies have used composites of crystal TiO₂ and microporous TiO₂ to enhance the mineralization efficiency of VOCs.

This study provides a replicable method to grow microporous TiO₂ onto anatase TiO₂ surface to form a nanocomposite exhibiting both high adsorption ability and photoactivity to photodegrade VOCs. Toluene was selected as model VOC to evaluate the mineralization ability of the prepared samples. Surface photovoltage spectroscopy (SPS) was used to study the effect of microporous TiO₂ growth on the separation of photogenerated charge carriers.

2. Materials and methods

2.1. Catalyst preparation

Microporous TiO₂ was grown onto anatase TiO₂ via a low-temperature hydrothermal method. Dodecylamine was used as the micropore-forming agent. For a typical synthesis, 0.5 g of anatase TiO₂ (Aladdin Chemistry, China) and 1.5 mL of dodecylamine (98%, Aladdin Chemistry, China) were added into 60 mL of absolute ethyl alcohol (99.5%, Aladdin Chemistry, China) followed by an ultrasound for 15 min. Titanium(IV) tetrabutoxide (3.45 mL, 99%, Aladdin Chemistry, China) in 60 mL absolute ethanol was added dropwise to the ethanol dispersion of the anatase TiO₂ particles under continuous stirring. Afterwards, 20 mL of deionized water

was added into the suspension, and the mixture was stirred for 2 h. The mixture was subsequently transferred into an autoclave with Teflon lining and heated at 90 °C for 24 h. After naturally cooling to room temperature, the solution was centrifuged. Dodecylamine in the solid was removed by stirring the solid in ethanol-HCl solution. The solid was subsequently washed with deionized water to remove the adsorbed HCl and dried at 60 °C in an oven. The obtained material was named micropore-anatase TiO₂ composite (MA). The theoretical yield ratio of microporous TiO₂ to anatase TiO₂ was 8:5 in MA. The microporous TiO₂ (M-TiO₂) was synthesized following exactly the same process, except addition of anatase TiO₂. Other details of the synthesis method were presented in our previous reports [22,23]. Degussa P25 was used as control photocatalyst.

2.2. Photocatalytic experiment

The setups for the adsorption and photocatalytic experiments consist of a gas tank, reactor, and GC (9790II, Fuli instrument, China), as shown in Fig. S1. Each part was connected by a Teflon tube with an inner diameter of 6 mm. The whole system was airtight, and the total volume is 21.4 L. The air in the system was circulated by two air pumps. The flows in the reactor-gas tank and the GC-gas tank were 1 and 150 mL/min, respectively. The reactor consisted of a quartz tube surrounded by four UV lamps (8W, central emission wavelength of 254 nm; the secondary wave at 183 nm was filtered). The distance between each UV lamp and quartz tube was 3 cm. The reactor and UV lamps were placed in a dark box. The samples were dispersed in ethanol and coated on the inner surface of the quartz tube by rotating in an oven at 60 °C. The coating area is 97 cm². The mass of the samples used in photocatalytic experiments and adsorption experiments was 20 ± 0.1 and 70 ± 0.1 mg, respectively. All of the samples were dried at 60 °C for 4 h before using. Highly pure air mixed with 81% N₂ and 21% O₂ (99.999%) flowed through a water blow bottle and thoroughly replaced the gas in the system before each experiment. The relative humidity (RH) was detected by a humidity meter (DT-616CT, CEM, China). The initial RH in the gas tank was adjusted to 50%. Toluene (99.5%, Aladdin Chemistry, China) was chosen as model VOC and injected into the gas tank. The valves at each end of the reactor were closed, and the valve of the bypass was kept open until toluene concentration reached up to 5.5 mg/m³. Afterwards, the valves at each end of the reactor were opened and the bypass was closed to conduct the experiments. The steps in adsorption experiments are similar to those in the photocatalytic experiments, except for UV irradiation. Gas was circulated between the gas tank and the quantitative rings (1 mL) of GC by a gas pump. The GC was equipped with two flame ionization detectors and a methane converter to detect the concentrations of toluene and CO₂. The GC automatically detected the gas in the quantitative rings every 8 min. All of the measurements were repeated three times.

2.3. Characterization of catalysts

N₂ adsorption/desorption was measured using an Autosorb-iQ2-MP Surface Area Analyzer (Quantachrome, USA). The specific surface area (S_{BET}), pore volume, average pore size, microporous surface area, external surface area, and pore size distribution were calculated by the software ASiQWin (Quantachrome, USA). X-ray diffraction (XRD) was performed using a D8 Advance (Bruker, Germany) with Cu K α radiation ($\Delta 2\theta = 0.02^\circ$, $\lambda = 0.15406$ nm). A transmission electron microscope (TEM, JEM-2100, JEOL, Japan) was used to observe the morphology of the nanostructured samples at an accelerating voltage of 200 kV. The surface composition of the prepared samples was analyzed by X-ray photoelectron spectroscopy (XPS, PHI Quantera II, Japan) with Al-K α as X-ray source. The setup was evacuated to the pressure of 6×10^{-6} Pa before

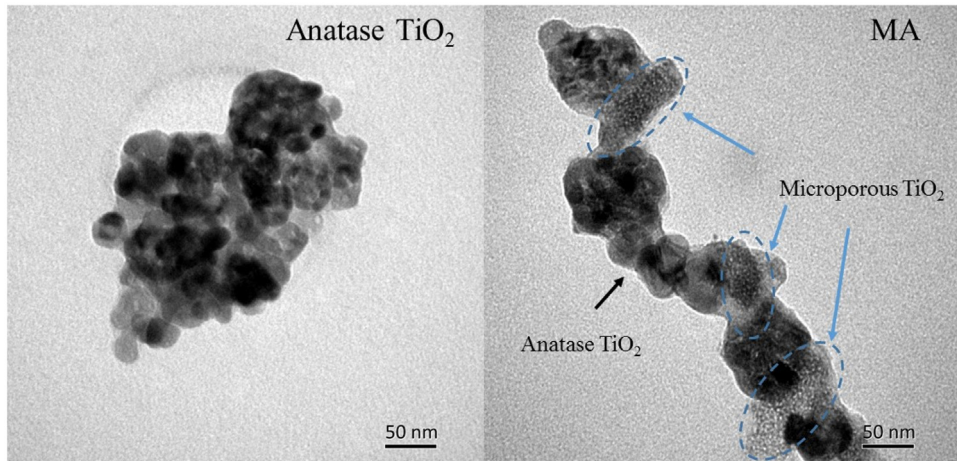


Fig. 1. Transmission electron microscopy images of anatase TiO_2 and MA.

Table 1

Structural properties of the tested nanocatalysts.

Samples	S_{BET} (m^2/g)	Pore volume (mL/g)	Average pore size (nm)	Microporous surface area (m^2/g)	External surface area (m^2/g)
MA	241	0.362	4.07	108	133
M- TiO_2	731	0.641	1.25	653	77.7
Anatase TiO_2	92.6	0.416	10.3	–	92.6
P25	50.2	0.464	35.4	–	50.2

the test. The XPS curves were calibrated by adventitious carbon signal at 284.6 eV. SPS was used to estimate the separation efficiency and transfer direction of photogenerated charge carriers. The SPS setup consisted of a 500 W xenon lamp (LSB-X500, Zolix, China), a monochromator (Omni-λ300, Zolix, China), a light chopper (SR540, Stanford Research Systems, USA), a photovoltaic cell, a lock-in amplifier (SR830, Stanford Research Systems, USA), and a computer (Fig. S2). The chopping frequency was 23 Hz. The samples were placed between an ITO electrode and a Cu electrode in the photovoltaic cell. The software Zolixscan designed by Zolix company was used to output data and to control the monochromator and lock-in amplifier. The wavelength of incident light was start from 450 nm. All the SPS experiments were conducted in a room with constant temperature of 25 °C and RH of 50%.

3. Results and discussion

3.1. TEM measurement

The micromorphology of the prepared TiO_2 was investigated using TEM. Fig. 1A shows that anatase TiO_2 consisted of aggregated nanoparticles with an average diameter of approximately 30 nm. Fig. 1B shows a large number of bright spots, indicating the abundance of micropores; similar microporous morphology was observed in the TEM image of M- TiO_2 (Fig. S3). Following the synthesis strategy presented in this paper, we have successfully grown microporous TiO_2 on the surface of anatase TiO_2 nanoparticles, forming a composite (MA). The microporous TiO_2 and anatase TiO_2 combined closely and homogeneously.

Earlier works [22,23] showed that crystal TiO_2 demonstrates a relatively high photoactivity but low adsorption ability, whereas microporous TiO_2 displayed remarkable adsorption ability for VOC gas but relatively low photoactivity. MA consisted of anatase TiO_2 and microporous TiO_2 , indicating a good performance in both adsorption and photocatalytic oxidation. Moreover, instead of encapsulating anatase TiO_2 particles, the newly formed microporous TiO_2 only covered part of the surface of anatase TiO_2 ,

exposing both the surfaces of anatase TiO_2 and microporous TiO_2 to the atmosphere, resulting in their direct interaction with air pollutants.

3.2. N_2 adsorption and desorption measurement

N_2 adsorption-desorption isotherms were analyzed to estimate the pore structure of MA, M- TiO_2 , anatase TiO_2 , and P25. S_{BET} was calculated using the Brunauer–Emmett–Teller method [24]. The external surface area and micropore area were calculated using the t-plot method developed by Lippert and deBoer [25,26]. Table 1 summarizes the S_{BET} , pore volume, average pore size, micropore area, external surface area, and micropore volume of the prepared samples. As listed in Table 1, S_{BET} of the materials decreased in the following order: M- TiO_2 > MA > anatase TiO_2 > P25. M- TiO_2 showed the largest surface area of 731 m^2/g , with a micropore area accounting for 89.3% of S_{BET} . After the microporous TiO_2 grew onto the surface of anatase TiO_2 , S_{BET} of the catalyst increased by 160.1%. Anatase TiO_2 , with an average pore size of 10.3 nm and contains no micropore area, showed a typical mesoporous structure. The average pore size of MA decreased to 4.07 nm compared with anatase TiO_2 and displayed a micropore area of 108 m^2/g . This result indicated that MA was not a typical mesoporous or microporous material. To further identify the pore structure of the prepared materials, we calculated the pore size distribution of MA and anatase TiO_2 by using density functional theory (DFT) with N_2 on carbon as calculation model. Fig. 2 shows that the pore widths of both MA and anatase TiO_2 were not uniform. MA showed two new sharp peaks at 1.8 and 4.1 nm compared with anatase TiO_2 . This result proved that the successfully grown microporous TiO_2 induced microporous structure and significantly increased the amount of pores with pore sizes of <5 nm in the catalyst. The pore width of 1.8 nm was higher than the average pore size of M- TiO_2 (Table 1). This result demonstrates that the pore size of microporous TiO_2 increased during its growth. The volume of pores with sizes of >5 nm was slightly lower in MA than in anatase TiO_2 ,

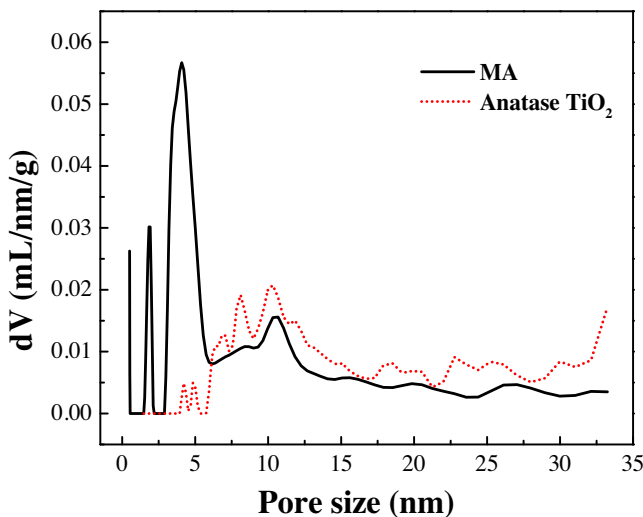


Fig. 2. Pore size distribution of MA and anatase TiO_2 calculated from N_2 adsorption-desorption isothermal curves by using the NovaWin2 software and DFT.

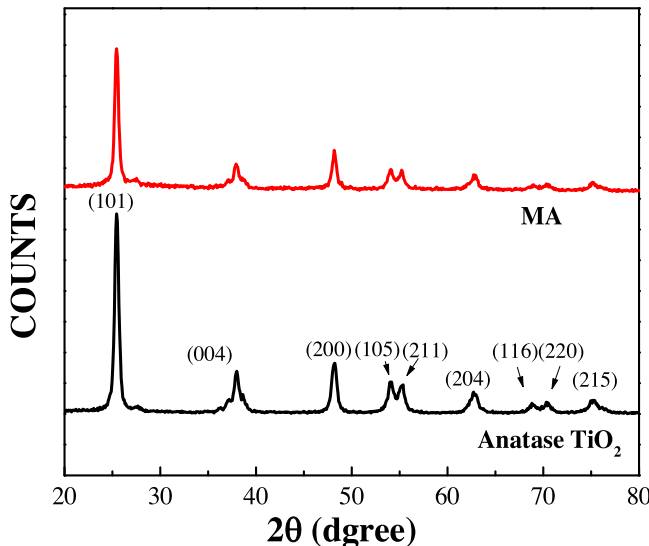


Fig. 3. XRD patterns of MA and anatase TiO_2 .

suggesting that part of microporous TiO_2 filled the mesopores of anatase TiO_2 . In addition, no micropore was observed in P25.

The amount of adsorption sites and catalytic sites on catalyst surface increases with surface area. Hay and his coauthors [27] states that increases in overall surface area are theorized to reduce the deactivation caused by adsorbed intermediates and increase the lifetime of the catalyst. Moreover, the micropore filling significantly improves the adsorption capacity of materials for low concentration of VOCs, whereas mesopores provide a higher transfer rate of gases compared with micropores [21,28]. Growth of microporous TiO_2 on anatase TiO_2 obviously increased the surface area and constructed microporous-mesoporous structure. This structure modification may enhance the adsorption of low VOC concentration, optimizing photocatalytic oxidation.

3.3. XRD measurement

The crystal phase of the prepared samples was analyzed by XRD. Fig. 3 shows that the peaks of the MA and anatase TiO_2 are indexed to the identical crystal planes of anatase TiO_2 , indicating that the growth of M- TiO_2 did not change the crystal phase. The peak inten-

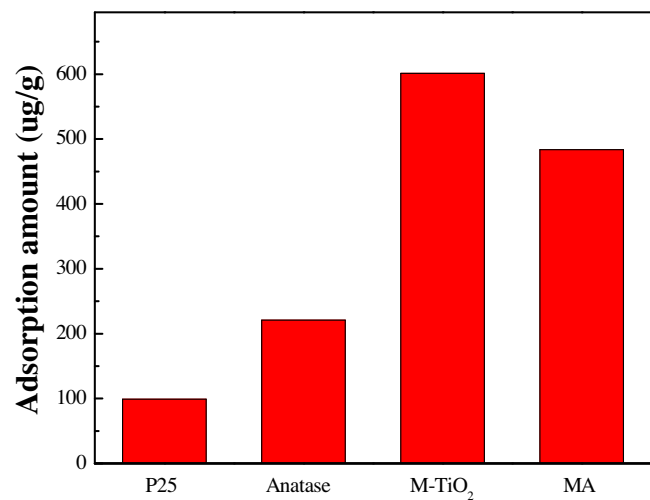


Fig. 4. Equilibrium amount of toluene adsorbed by the tested catalysts.

sity of MA was lower than that of anatase TiO_2 . This phenomenon is largely attributed to the amorphous pattern of M-TiO₂, as shown in Fig. S4.

Photocatalytic activity is usually increased with the degree of crystallinity owing to the few bulk defects and low number of $e^- - h^+$ pair recombination [29]. In our previous work [23], we improved the crystallinity of microporous TiO_2 via hydrothermal method and obtained microporous anatase TiO_2 sample. However, micropores collapse easily as heating temperature reaches $>115^\circ\text{C}$, and the degree of crystallinity of the obtained microporous anatase TiO_2 is obviously lower than that of MA. In this case, the MA sample obtained displays both high degree of crystallinity and microporous structure.

3.4. Materials for toluene adsorption

The amount of adsorbed toluene was measured through a static adsorption experiment. The initial toluene concentration was 5.5 mg/m^3 , and the final concentration was measured after 40 min of adsorption in the dark. Fig. 4 shows that the amount of adsorbed toluene over the prepared samples decreased in the following order: M-TiO₂ > MA > anatase TiO_2 > P25, similar to the trend for S_{BET} . After microporous TiO_2 grew onto anatase TiO_2 , the amount of adsorbed toluene became 2.2 times higher than that adsorbed on anatase TiO_2 . S_{BET} of M-TiO₂ was 3.0 times larger than that of MA, whereas the amount of adsorbed toluene over M-TiO₂ was only 1.2 times higher than that adsorbed over MA. This phenomenon is largely attributed to the difference in pore size distribution of MA and M-TiO₂. The small pore size of 1.25 nm of M-TiO₂ created a strong adsorption potential and thus limiting the diffusion of toluene in pores. After 40 min, part of micropores inside M-TiO₂ remained unfilled with toluene. Instead, the pores of MA consisted both of micropores (1.8 nm) and mesopores ($>4 \text{ nm}$), which considerably increased the diffusion of toluene and made the adsorption equilibrium easier to reach.

3.5. Photocatalytic degradation of toluene

No decrease in toluene concentration and increase in CO_2 concentration were observed in the control experiments without either the photocatalysts or UV light illumination. Fig. 5A shows that toluene concentration over MA and M-TiO₂ decreased more quickly than that over anatase TiO_2 and P25. Anatase TiO_2 and P25 took 60 min to reduce toluene to an undetectable concentration, whereas MA and M-TiO₂ required 45 min only. Adsorption and

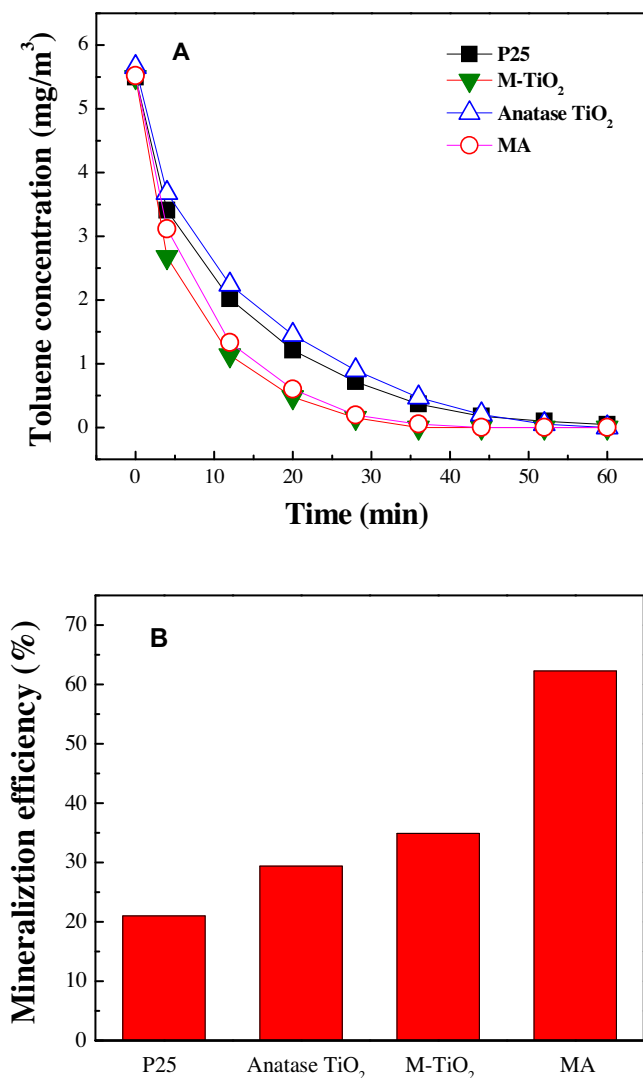


Fig. 5. Removal curves (A) and mineralization efficiencies (B) of toluene over prepared samples.

photooxidation both reduced toluene concentration. For toluene at a low concentration of 5.5 mg/m³, adsorption was the rate-determining step in photocatalytic removal of toluene. MA and M-TiO₂ both showed remarkable adsorption ability, leading in better removal rate of toluene compared with that of anatase TiO₂ and P25.

Determining the amount of the removed VOCs that are converted into CO₂ and H₂O is more important because harmful byproducts are generated during the photocatalytic process. Hence, we measured the concentrations of generated CO₂ and calculated the mineralization efficiency (φ , %) by using Eq. (1):

$$\text{Mineralization efficiency} : \varphi = \frac{C_0}{3.34C_0} \times 100 \quad (1)$$

where C₀ is the initial gas phase toluene concentrations expressed in mg m⁻³. C₀ is the concentration of generated CO₂ after 60 min of photocatalytic oxidation and expressed in mg m⁻³. The amount of theoretically generated CO₂ is represented by 3.34C₀.

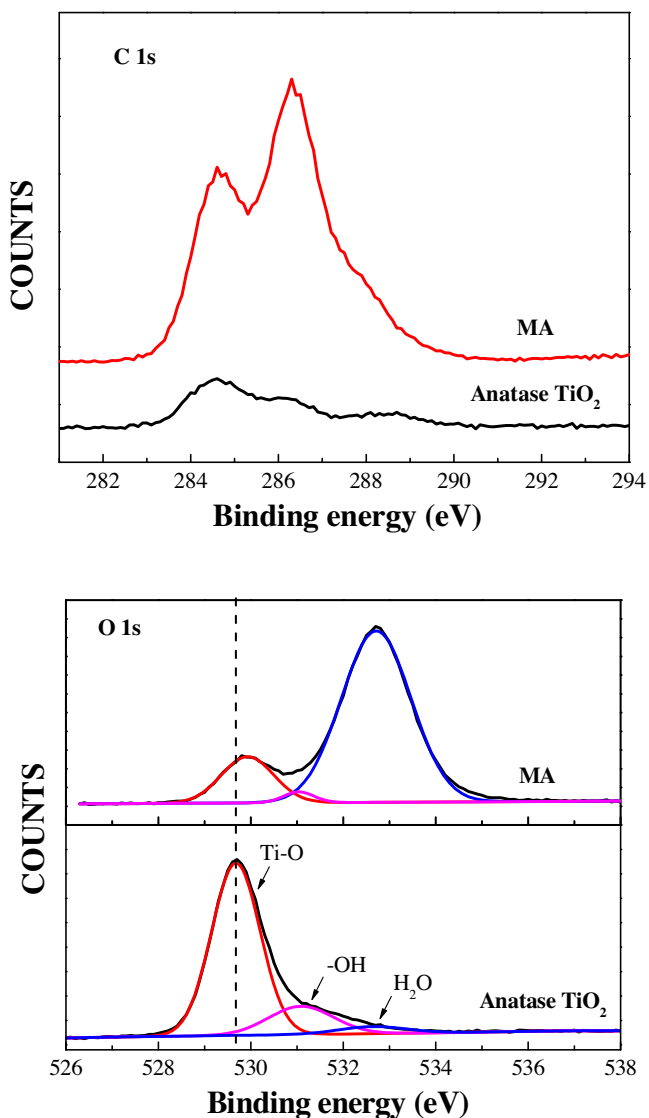
Fig. 5B shows that the mineralization efficiencies of toluene decreased in the following order: MA > M-TiO₂ > anatase TiO₂ > P25. After microporous TiO₂ and anatase TiO₂ were combined, the mineralization efficiency of toluene significantly increased by 78.4% and 111.9% compared with that of M-TiO₂ and anatase TiO₂,

respectively. This result clearly indicated the synergistic effect of microporous TiO₂ and anatase TiO₂ in MA. M-TiO₂, which exhibits an amorphous pattern, should demonstrate a very low photoactivity. However, M-TiO₂ exhibited relatively high removal rate and mineralization efficiency. This observation can be explained by two points: (i) M-TiO₂ containing large micropore area concentrated toluene at photocatalytic sites and thus increased the injection of photogenerated charge carriers to the adsorbed toluene. Nakamura and Nakato reported that photocurrent largely increases if organic compounds directly reacts with photo-generated holes, whereas photocurrent hardly increases if an indirect reaction via the intermediates of water photoxidation occurs [30]; and (ii) given the strong adsorption potential in micropores, the intermediates formed in micropores during photooxidation were considerably difficult to release and showed a long residence time at the catalyst surface. After microporous TiO₂ grew on anatase TiO₂, the superiority of the obtained nanocomposite is similar to that of M-TiO₂.

3.6. Characterization of the surface elements on the catalysts surface

XPS experiments were conducted to study the chemically and physically adsorbed species at MA and anatase TiO₂ surface. Prior to conducting XPS measurements, the samples were degassed at a base pressure of 6×10^{-6} Pa for 4 h. Fig. 6 shows the C1 s and O1 s spectra of MA and anatase TiO₂ and Fig. S5 shows the whole spectra and Ti2P spectra. Carbon is an abundant element in nature and always detected by XPS. However, the intensity of C1s peak of MA was much higher than that of the C1s peak of anatase TiO₂. To quantify the difference in the amount of adsorbed carbon on the surface of the two samples, we calculated the ratios of the intensity of C1s peak at 286.4 eV to the intensity of Ti2p peak at 458.4 eV. The C/Ti ratio of MA was 1.88, whereas the ratio of anatase TiO₂ was only 0.02. This result clearly showed that the amount of adsorbed carbon species on MA surface was significantly larger than that of anatase TiO₂. Considering the effect of degassing treatment prior to XPS measurements, we speculate that the adsorbed organic compounds are much difficult to desorb from the MA surface than from the anatase TiO₂ surface. Compared with anatase TiO₂, MA displayed a microporous structure. When the size of micropores was <2 nm, the adsorption potentials of adjacent pore walls overlapped, enhancing the attraction between organic compounds and the material surface. As toluene and its intermediates showed a long residence time at MA surface, they were more likely to be mineralized into CO₂ and H₂O.

The O1s spectra of MA and anatase showed three peaks. The peaks at 529.9, 531.0, and 532.7 eV are indexed to oxygen from TiO₂, to chemically bonded H₂O (−OH), and to physically adsorbed H₂O, respectively [31–33]. In most cases, the physically adsorbed H₂O can be easily removed from the sample surface through degassing preparation treatment. The peak area assigned to the physically adsorbed H₂O only accounted for 4.4% of O1s peak of anatase TiO₂, whereas it counted for 81.3% for MA. This result proved that not only organic compounds were difficult to release from MA surface but also H₂O molecules. H₂O can react with photogenerated electron–hole pairs and transform into radical species, such as ·OH and HO₂[·], which are beneficial for oxidation of VOCs [34,35]. The quick diffusion of products such as CO₂ and H₂O is also important to promote the reaction. Therefore, too strong adsorption should not be beneficial to toluene mineralization. However, the XPS and toluene degradation results showed the growth of microporous TiO₂ enhanced both the adsorption of organic compounds and H₂O and the mineralization of toluene. This suggests that micropores with pore size larger than 1.8 nm would not obviously limit the diffusion of CO₂ and H₂O. Moreover, the peak of oxygen from TiO₂ shifted to higher binding energy by 0.2 eV after microporous TiO₂

Fig. 6. C1s and O1s XPS of MA and anatase TiO₂.

grew on anatase TiO₂, indicating that microporous TiO₂ induced oxygen vacancy to the catalyst. Oxygen vacancy usually acts as the adsorption and reaction sites of O₂ and pollutants, enhancing the separation of photogenerated charge carriers [36–38]. Pham and Wang reported that oxygen vacancies and their defective states provide hopping channels, which are beneficial for hole conduction [39]. Based on the above statement, MA surface had oxygen vacancy and strongly attracted organic compounds and H₂O, possibly greatly contributing to photocatalytic mineralization of toluene.

3.7. Separation behavior of photogenerated charge carriers at the catalysts surface

SPV and the corresponding phase spectrum were measured to study the effect of the growth of microporous TiO₂ on the separation efficiency and transfer direction of the photogenerated charge carriers. The spectra were obtained by scanning from low to high photon energies $h\nu$. The drop in SPV value as the light wavelength below 350 nm is due to the decrease of light intensity of xenon lamp and the light adsorption by ITO glass. Fig. 7 shows that the SPV at M-TiO₂ surface was nearly undetectable (0.055 mV), whereas anatase TiO₂ showed an SPV of 1.12 mV in the ultraviolet region. This observation can be easily explained by the difference in crystallinity

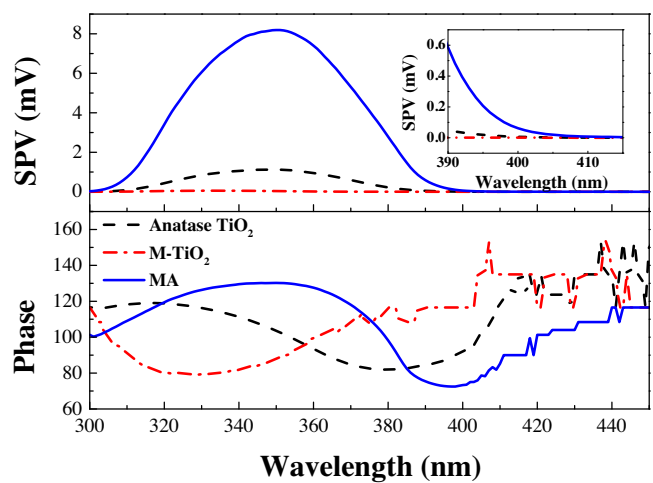


Fig. 7. Surface photovoltage (A) and phase spectra (B) of the prepared samples.

between the two catalysts. Interestingly, after microporous TiO₂ grew onto anatase TiO₂, the SPV of MA sharply increased to 8.19 mV, indicating that microporous TiO₂ growth significantly improved the separation efficiency of photogenerated electrons and holes in the near surface region of the catalysts. The inset in Fig. 7 shows that MA showed a weak signal response at the 400–410 nm region. Linear regressions on the straight line portion of the SPV data between 350 and 400 nm were performed to obtain the x intercepts. The intercepts of MA, anatase TiO₂, and M-TiO₂ were 391.2, 385.5, and 367.4 nm, respectively. The light wavelengths can be transferred to light energy to indicate the bandgap of the prepared samples. Therefore, the bandgap of MA, anatase TiO₂, and M-TiO₂ were 3.17, 3.22, and 3.38 eV. The bandgap of the anatase TiO₂ used in this study was kept consistent with a typical value of anatase TiO₂ bandgap. M-TiO₂ showed a relatively high bandgap because of its amorphous pattern, consistent with the previous results on amorphous TiO₂ [40]. However, after M-TiO₂ grew onto anatase TiO₂, the bandgap of the catalyst decreased by 0.05 eV. As shown in Ti2p and O1s XPS spectra (Figs. S5 and 6), the binding energy of Ti and O from Ti-O in MA was 0.1 and 0.2 eV higher than that in anatase TiO₂, respectively. Given that the microporous TiO₂ grew on anatase TiO₂ surface, the blue shifts in the binding energy were largely caused by coated microporous TiO₂. Thus, the conduction band edge and valence band edge of the coated microporous TiO₂ were lower than those of anatase TiO₂. These results indicated that the reduction in bandgap caused by the growth of microporous TiO₂ is largely attributed to electron leaping from the valence band of anatase TiO₂ to the conduction band of coated microporous TiO₂ at the interface of the two composites materials.

Given that the phase spectrum of nanomaterials is controlled by many kinds of carrier transition processes, phase spectrum is usually analyzed in the region around the bandgap to determine the band bending direction. Generally, the phase value will shift to $\pm 0^\circ$ ($\pm 180^\circ$) as $h\nu$ increased in the case of upward band bending (downward band bending) [41,42]. Fig. 7 shows that in the region around the bandgap of M-TiO₂ (367.4 nm) and anatase TiO₂ (385.5 nm), the phase value of M-TiO₂ decreased with increasing $h\nu$, whereas the phase value of anatase TiO₂ showed the opposite trend. This result indicated that the bands of M-TiO₂ and anatase TiO₂ bended upward and downward in the near surface region, respectively. Given that the band bending direction is determined by Fermi levels of the sample and ITO glass, the phase results proved that the Fermi levels decreased in the following order: M-TiO₂ > ITO > anatase TiO₂. Therefore, when M-TiO₂ and anatase TiO₂ were combined in MA, the band near the interface would bend upward in the microporous side and downward in the anatase side.

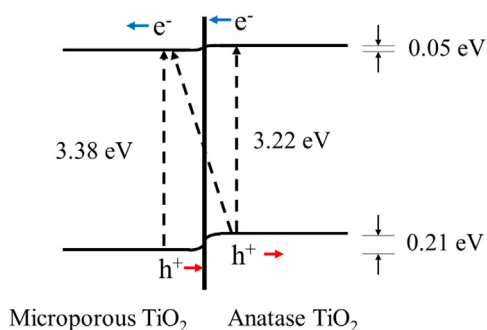


Fig. 8. Primary photoprocess at the interface of microporous TiO_2 and anatase TiO_2 (dotted arrow: band to band leaps of electrons; solid arrows: transfer directions of photogenerated charge carriers at the interface region).

Fig. 8 shows the primary photoprocess at the interface between microporous TiO_2 and anatase TiO_2 . The bandgaps of M- TiO_2 and anatase TiO_2 were 3.38 and 3.22 eV, respectively. The XPS results show that the conduction and valence band edges of the coated microporous TiO_2 were lower than those of the anatase TiO_2 in MA. Therefore, electrons could leap from the valence band of anatase TiO_2 to the conduction band of microporous TiO_2 via light irradiation with energy lower to 3.17 eV. The SPV proves that the Fermi level of M- TiO_2 was higher than that of anatase TiO_2 . As the M- TiO_2 grew on anatase TiO_2 surface, a homojunction was constructed at the interface. The free electrons flew from the microporous TiO_2 to the anatase TiO_2 until the Fermi levels of microporous TiO_2 and anatase TiO_2 aligned. Under equilibrium, the microporous TiO_2 was positively charged and the anatase TiO_2 was negatively charged at the interface. This phenomenon formed an electric field at the interface, making the band edges of microporous TiO_2 to bend upward toward the interface, whereas the band of anatase TiO_2 bent downward toward the interface. Under light irradiation, the photogenerated electrons at the interface region transferred from anatase TiO_2 to the microporous TiO_2 , whereas the photogenerated holes flew to the opposite direction driven by the interface electric field. These phenomena significantly enhanced the separation of photogenerated charge carriers, improving the photoactivity of the catalyst.

4. Conclusion

Microporous TiO_2 grew on the surface to anatase TiO_2 to form homojunction-adsorption layer, resulting in optimized adsorption ability and photoactivity of the catalyst for photocatalytic mineralization of VOCs. After growth of microporous TiO_2 , the mineralization efficiency of the newly formed catalyst, MA, increased by 78.4% and 111.9% compared with that of M- TiO_2 and anatase TiO_2 , respectively. This result is mainly attributed to two reasons: 1) growth of microporous TiO_2 onto anatase TiO_2 surface significantly enlarged the surface area and induced microporous structure. Therefore, toluene was concentrated near the photocatalytic sites and the intermediates were difficult to desorb from the catalyst surface to gas phase before being mineralized. 2) A homojunction structure formed at the interface of microporous TiO_2 and anatase TiO_2 , improving the separation of photogenerated charge carriers. Thus, growth of microporous TiO_2 on anatase TiO_2 significantly enhanced toluene mineralization. MA is possibly an ideal catalyst for degradation of low concentration of VOCs.

Acknowledgements

Financial support by Jiangsu Province Science Foundation for Youth (BK20150126), the Opening Project of Key Laboratory

of Green Chemistry of Sichuan Institutes of Higher Education (LZJ14203), Fundamental Research Funds for the Central Universities (JUSRP51512), and Jiangnan University Science Foundation (JUSRP11522) is greatly appreciated.

Appendix A. Supplementary data

Supplementary data associated with this article can be found, in the online version, at <http://dx.doi.org/10.1016/j.apcatb.2016.09.041>.

References

- [1] M. Kampa, E. Castanas, Environ. Pollut. 151 (2008) 362–367.
- [2] D. Johnson, S.R. Utembe, M.E. Jenkin, Atmos. Chem. Phys. 6 (2006) 419–431.
- [3] R.-J. Huang, Y. Zhang, C. Bozzetti, K.-F. Ho, J.-J. Cao, Y. Han, K.R. Daellenbach, J.G. Slowik, S.M. Platt, F. Canonaco, P. Zotter, R. Wolf, S.M. Pieber, E.A. Brun, M. Crippa, G. Ciarelli, A. Piazzalunga, M. Schwikowski, G. Abbaspazadeh, J. Schnelle-Kreis, R. Zimmermann, Z. An, S. Szidat, U. Baltensperger, I. El Haddad, A.S.H. Prevot, Nature 514 (2014) 218–222.
- [4] Q. Zhang, B. Yuan, M. Shao, X. Wang, S. Lu, K. Lu, M. Wang, L. Chen, C.C. Chang, S.C. Liu, Atmos. Chem. Phys. 14 (2014) 6089–6101.
- [5] B. Liu, H.M. Chen, C. Liu, S.C. Andrews, C. Hahn, P.D. Yang, J. Am. Chem. Soc. 135 (2013) 9995–9998.
- [6] X.F. Qian, D.T. Yue, Z.Y. Tian, M. Reng, Y. Zhu, M. Kan, T.Y. Zhang, Y.X. Zhao, Appl. Catal., B 193 (2016) 16–21.
- [7] L.G. Devi, R. Kavitha, Appl. Catal., B 140 (2013) 559–587.
- [8] J. Reszczynska, T. Grzyb, J.W. Sobczak, W. Lisowski, M. Gazda, B. Ohtani, A. Zaleska, Appl. Catal., B 163 (2015) 40–49.
- [9] J.C. Liu, H.W. Bai, Y.J. Wang, Z.Y. Liu, X.W. Zhang, D.D. Sun, Adv. Funct. Mater. 20 (2010) 4175–4181.
- [10] Y.M. Kim, S. Harrad, R.M. Harrison, Environ. Sci. Technol. 35 (2001) 997–1004.
- [11] M. Weng, L. Zhu, K. Yang, S. Chen, J. Hazard. Mater. 164 (2009) 700–706.
- [12] C. Chi, W. Chen, M. Guo, M. Weng, G. Yan, X. Shen, Atmos. Environ. 132 (2016) 85–90.
- [13] J. Lyu, L. Zhu, C. Burda, Catal. Today 225 (2014) 24–33.
- [14] M. Sleiman, C. Ferronato, J.-M. Chovelon, Environ. Sci. Technol. 42 (2008) 3018–3024.
- [15] I. Jansson, S. Suarez, F.J. Garcia-Garcia, B. Sanchez, Appl. Catal., B 178 (2015) 100–107.
- [16] C.H. Ao, S.C. Lee, Appl. Catal., B 44 (2003) 191–205.
- [17] N. Takeda, T. Torimoto, S. Sampath, S. Kuwabata, H. Yoneyama, J. Phys. Chem. 99 (1995) 9986–9991.
- [18] J. Lee, M.C. Orilall, S.C. Warren, M. Kamperman, F.J. Disalvo, U. Wiesner, Nat. Mater. 7 (2008) 222–228.
- [19] W. Dong, Y. Sun, C.W. Lee, W. Hua, X. Lu, Y. Shi, S. Zhang, J. Chen, D. Zhao, J. Am. Chem. Soc. 129 (2007) 13894–13904.
- [20] Z.M. Wang, K. Kaneko, J. Phys. Chem. B 102 (1998) 2863–2868.
- [21] Y. Hanzawa, T. Suzuki, K. Kaneko, Langmuir 10 (1994) 2857–2859.
- [22] J. Lv, L. Zhu, Environ. Technol. 34 (2013) 1447–1454.
- [23] J. Lyu, L. Zhu, C. Burda, Chemcatchem 5 (2013) 3114–3123.
- [24] S. Brunauer, P.H. Emmett, E. Teller, J. Am. Chem. Soc. 60 (1938) 309–319.
- [25] P. Voogd, J.J.F. Scholten, H. van Bekkum, Colloids Surf. 55 (1991) 163–171.
- [26] B.C. Lippens, J.H. de Boer, J. Catal. 4 (1965) 319–323.
- [27] S.O. Hay, T. Obree, Z. Luo, T. Jiang, Y.T. Meng, J.K. He, S.C. Murphy, S. Suib, Molecules 20 (2015) 1319–1356.
- [28] J. Du, X.Y. Lai, N.L. Yang, J. Zhai, D. Kisailus, F.B. Su, D. Wang, L. Jiang, Acs Nano 5 (2011) 590–596.
- [29] V. Puddu, H. Choi, D.D. Dionysiou, G.L. Puma, Appl. Catal., B 94 (2010) 211–218.
- [30] R. Nakamura, T. Tanaka, Y. Nakato, J. Phys. Chem. B 108 (2004) 10617–10620.
- [31] Z. Song, J. Hrbek, R. Osgood, Nano Lett. 5 (2005) 1327–1332.
- [32] N. Kruse, S. Chenakin, Appl. Catal., A 391 (2011) 367–376.
- [33] H. Perron, J. Vandenne, C. Domain, R. Drot, J. Roques, E. Simoni, J.J. Ehrhardt, H. Catalette, Surf. Sci. 601 (2007) 518–527.
- [34] P. Pichat, Appl. Catal., B 99 (2010) 428–434.
- [35] P. Salvador, J. Phys. Chem. C 111 (2007) 17038–17043.
- [36] M.A. Henderson, W.S. Epling, C.L. Perkins, C.H.F. Peden, U. Diebold, J. Phys. Chem. B 103 (1999) 5328–5337.
- [37] C.L. Muñich, Y. Zhou, A.M. Holder, A.W. Weimer, C.B. Musgrave, J. Phys. Chem. C 116 (2012) 10138–10149.
- [38] Q. Wu, R. van de Krol, J. Am. Chem. Soc. 134 (2012) 9369–9375.
- [39] H.H. Pham, L.-W. Wang, Phys. Chem. Chem. Phys. 17 (2015) 541–550.
- [40] D. Chandra, A. Bhaumik, Microporous Mesoporous Mater. 112 (2008) 533–541.
- [41] T. Ivanov, V. Donchev, K. Germanova, K. Kirilov, J. Phys. D: Appl. Phys. 42 (2009) 1–7.
- [42] V. Donchev, K. Kirilov, T. Ivanov, K. Germanova, Mater. Sci. Eng., B 129 (2006) 186–192.